



HAL
open science

Size and structure of hexanuclear plutonium oxo-hydroxo clusters in aqueous solution from synchrotron analysis

Thomas Dumas, Matthieu Viot, Denis Menut, Christelle Tamain, Cyril
Micheau, Sandrine Dourdain, Olivier Diat

► To cite this version:

Thomas Dumas, Matthieu Viot, Denis Menut, Christelle Tamain, Cyril Micheau, et al.. Size and structure of hexanuclear plutonium oxo-hydroxo clusters in aqueous solution from synchrotron analysis. *Journal of Synchrotron Radiation*, 2022, 29 (1), pp.30. 10.1107/S1600577521012005 . cea-03630418

HAL Id: cea-03630418

<https://cea.hal.science/cea-03630418>

Submitted on 5 Jul 2022

HAL is a multi-disciplinary open access archive for the deposit and dissemination of scientific research documents, whether they are published or not. The documents may come from teaching and research institutions in France or abroad, or from public or private research centers.

L'archive ouverte pluridisciplinaire **HAL**, est destinée au dépôt et à la diffusion de documents scientifiques de niveau recherche, publiés ou non, émanant des établissements d'enseignement et de recherche français ou étrangers, des laboratoires publics ou privés.



Distributed under a Creative Commons Attribution 4.0 International License

Size and structure of hexanuclear Plutonium oxo-hydroxo clusters in aqueous solution from synchrotron analysis.

Thomas Dumas^{1*}, Matthieu Virost^{2*}, Denis Menut³, Christelle Tamain¹, Cyril Micheau², Sandrine Dourdain², Olivier Diat².

¹ CEA, DES, ISEC, DMRC, Univ Montpellier, Marcoule, France

² CEA, DES, ISEC, ICSM, Univ Montpellier, Marcoule, France

³ Synchrotron SOLEIL – L'Orme des Merisiers Saint-Aubin - BP 48 91192 Gif-sur-Yvette Cedex – France

Abstract

In this work, the size and shape of a water soluble hexanuclear plutonium cluster was probed by combining synchrotron Small Angle X-ray Scattering (SAXS) and Extended X-ray Absorption Fine Structure (EXAFS). A specific set-up coupling both techniques and dedicated to radioactive samples at the MARS beamline end station is described. The plutonium hexanuclear cores are well stabilized by the DOTA ligands and allows a good evaluation of the set-up to probe very small plutonium core. The experiment results show that, in spite of the constrained conditions avoided any risk of sample dispersion, the flux as well as the sample environment are optimized to get a very good signal over noise ratio and allowing to detect the formation of small plutonium aggregates in aqueous phases. The structure of the well-defined hexanuclear cluster has been confirmed by EXAFS measurements in solution and correlated to SAXS data processing and modeling. The iterative comparison of classical fit models (Guinier or sphere form factor) with the experimental results allowed a better interpretation of SAXS signal that will be relevant for future works in environmentally relevant conditions.

Introduction

Because plutonium is highly radiotoxic, it represents one of the major long-term risk in the nuclear waste management. To predict and control the plutonium behavior in various environmental conditions, thermodynamic models are currently developed to describe plutonium solubility and surface interactions. (Altmaier *et al.*, 2013; Geckeis *et al.*, 2013; Kersting *et al.*, 1999) Nevertheless, new experimental inputs are still necessary in order to improve the reliability of these models. Among them, any additional fundamental knowledge on the complex plutonium chemistry at the molecular scale is highly desirable for long term nuclear disposal safety. In this scope, and within the large variety of plutonium chemical and redox states, hydrolyzed forms of tetravalent plutonium are crucial objects to consider. Due to its high charge density in aqueous solution, the Pu⁴⁺ ion has a high tendency for hydrolysis reactions and can further polymerize through oxolation and/or ololation reactions. The intermediate clusters formed through these reactions can further condensate to yield colloidal plutonium nanoparticles which might enhance its mobility. (Dalodiere *et al.*, 2017; Gerber *et al.*, 2020; Micheau *et al.*, 2020; Neck *et al.*, 2007; Walther *et al.*, 2007; Walther & Denecke, 2013) Until now, the addition of complexing molecules was considered to limit the growth of colloids leading to smaller polynuclear species and affecting plutonium solubility in complexing humic acid conditions. (Marsac *et al.*, 2014) Even if analogous tetravalent cations can also form polynuclear clusters with different number of metallic cations M⁴⁺ in the nuclear core (Hennig *et al.*, 2012; Hennig *et al.*, 2017; Knope *et al.*, 2011; Takao *et al.*, 2012), only recent works have characterized small polynuclear plutonium clusters. Knope *et al.* (Knope & Soderholm, 2013) first revealed the formation of a solid Li₆[Pu₆(OH)₄O₄(H₂O)₆(HGly)₁₂]Cl₁₈·10.5 H₂O, which consists of a mixed hydroxo/oxo plutonium(IV) hexanuclear cluster. More recently, Tamain *et al.* (Tamain *et al.*, 2016; Tamain *et al.*, 2017) used visible and X-ray Absorption Spectroscopy (XAS) techniques to correlate solid state and solution structures of another hexanuclear complex exhibiting the same [Pu₆(OH)₄O₄]¹²⁺ core, stabilized with the polyamino carboxylic acid DOTA (1,4,7,10-tetraazacyclododecane-1,4,7,10-tetraacetic acid). Visible absorption and reflectance spectra as well as Extended X-ray Absorption Fine Structure (EXAFS) measurements confirmed the stability of the hexanuclear core from the solid state to the solution. However both spectroscopic approaches only provide plutonium centered information and indicate that the plutonium hexanuclear core is preserved in solution. To describe long range interactions in solution, Small Angle X-ray Scattering (SAXS) was applied in combination with EXAFS in aqueous solution. SAXS offers a complementary image of the plutonium species in solution. This technique was already used for other actinides polynuclear compounds characterization, in solution. For instance, SAXS was used on U oxo-clusters by Martin *et al.* to follow the U(IV) hydrolysis, condensation and growth up to the formation of U-38 clusters (Martin *et al.*, 2018). It was also applied to uranyl peroxo nanospheres (Falaise & Nyman, 2016) (Dembowski *et al.*, 2017; Zhang *et al.*, 2019) and even to the small hexanuclear uranium core clusters by Falaise *et al.* (Falaise *et al.*, 2017). Recently SAXS measurements became available for

plutonium samples at the MARS beamline and were used in combination with XAS to study plutonium colloids. (Micheau *et al.*, 2020) Although the molecular structure of the hexanuclear DOTA plutonium clusters are well identified by single crystal XRD and the ability of the mars beamline to perform SAXS measurements on plutonium colloids were previously demonstrated, this work take the opportunity to probe the more challenging hexanuclear core clusters of plutonium in aqueous solution. The idea of probing small hexanuclear cluster core of plutonium was twofold: (i) assign as a test the ability of this set-up to detect small and diluted object in aqueous solution, and propose a more detailed description of the set-up (ii) provide information on the external shape of hexanuclear plutonium clusters in solution, that were beforehand only defined by the first two coordination shell of plutonium atoms.

Material and Method:

Synthesis of the $[\text{Pu}_6(\text{OH})_4\text{O}_4(\text{H}_2\text{O})_8(\text{HDOTA})_4]$ cluster.

The plutonium DOTA hexanuclear cluster was synthesized as previously reported (Tamain *et al.*, 2016). 47 mg of protonated DOTA was dissolved in 400 μL of water (under heating) and 80 μL of HNO_3 1 $\text{mol}\cdot\text{L}^{-1}$ was added after complete dissolution of the ligand. The plutonium solution was added to the ligand one ($[\text{Pu}]/[\text{L}] = 1/5$). The solution was left overnight to give crystals of plutonium(IV) hexamer. The SAXS sample was prepared by dissolution of 2.3 mg of crystals in 1 M HNO_3 . The sample purity and concentration of 0.01 M (concentration of Pu involved in the hexamer) were checked using UV-Vis absorption spectroscopy in the visible range (400-800 nm) (see **Figure 1**). The spectrum collected in the visible range is identical to the one reported previously and insure the sample purity. The slight baseline deviation observed below 600 nm is related to a variation of HNO_3 concentration between the two samples.

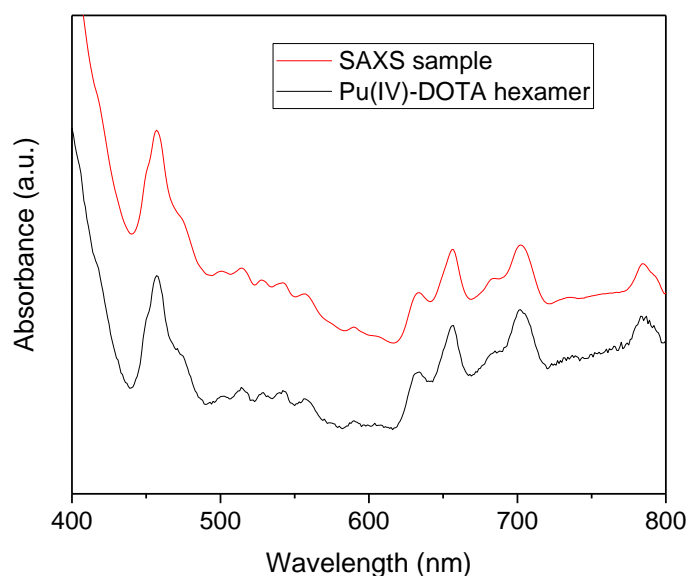


Figure 1: UV-Vis spectrum of the SAXS-XAFS sample compared to the Pu(IV)-DOTA-hexamer identified by single crystal XRD.

Measurement by synchrotron radiation and experimental set-up.

In this section, we shall give a brief summary of the design and the relevant characteristics of the Multi Analyses on Radioactive Samples (MARS) beamline at the synchrotron SOLEIL (Saint-Aubin, France). (LLorens *et al.*, 2014; Sitaud *et al.*, 2012), as well as presenting more specific developments making the beamline especially suitable for scattering experiments.

From its inception, MARS was designed to accommodate the wide-ranging scientific requirements of the radionuclide and actinide sciences (up to highly radioactive materials) covering areas from biology, environmental science through to advanced materials to directly characterize of the chemistry and microstructure with the use of synchrotron-based techniques. The beamline is licensed to receive samples with radioisotope activities up to 2 Million times their isotope specific European exemption limits and complies with all legal requirements and safety precautions to avoid contaminating aerosol dissemination and guarantee the public dose rate outside the beamline. It has successfully shown its flexibility by accommodating a wide array of diverse sample environments during its years of operation. (Bechade *et al.*, 2012; Menut *et al.*, 2015; Bechade *et al.*, 2013; LLorens *et al.*, 2014; Dumas *et al.*, 2018; Bengio *et al.*, 2020)

X-rays are sourced from a 1,71 T bending magnet providing a continuous spectrum of photons with a critical energy of 8,6 keV. A Double-Crystal Monochromator (Oxford Danfysik, Oxford, UK) allows tunable monochromatization in the continuous energy range 3.5 keV to 35 keV and horizontal focusing with a sagittal bender. The original feature of this DCM is its ability to exchange Si(111) and Si(220) crystals sets under vacuum to optimize the photon flux and energy resolution over the energy range. Two long mirrors are inserted before and after the DCM for high-energy harmonics rejection and to provide respectively a vertically collimated and focused beam. These mirrors consist of silicon blocks with two different reflective surfaces: a 60 mm width silicon uncoated strip for energy setup below 14 keV and a 50 mm width platinum coated strip (thickness 60 nm) for high energies. The X-ray beam at the second end-station of the MARS beamline (CX3), where were performed the scattering and absorption measurements described in the following, can be focused down to a 300 microns x 150 microns spot [full width at half-maximum (FWHM), horizontal (H) x vertical (V)] with the possibility to further microfocus the beam down to 15 x 15 microns on the second end-station in the reduced range 3,5 keV to 21 keV by inserting additional rhodium coated mirrors in the Kirkpatrick-Baez geometry). Two kind of 2-dimensionnal detectors (image plate or hybrid pixel) are available for the scattering and/or diffraction analyses which can be moved along the X-ray axis. Thus, depending on the energy used and the exact geometry of the scattering set up, the Q-range achievable may be adapted.

As SAXS is contingent on the accurate subtraction of all background scattering contributions (optical elements, windows, slits, air, ...), reducing the effects of parasitic scattering is vital not only to improve signal-to-noise ratios in the data but also to remove sources of scattering that may perturb the extraction

of structural parameters. The instrument background at MARS was reduced by a standard three-paired-slits collimator system where the first slits define the beam and adjust the flux, the second slits cut out the parasitic scattering fan coming from the optics and passing through the first pair of slits, and the third and last pair of slits remove the weaker secondary scattering produced by the second pair of slits. To further reduce this background, third slits are set-up by hybrid scattering slits from Xenocs (Sassenage, France). These scatterless slits are composed of heavy metal blades with Ge-monocrystal lateral edges oriented far from any Bragg peak position with respect to the incident beam. Based on comparison of the energy-dependent attenuation lengths of Ge, it actually offers the best attenuation of energies above 12 keV for synchrotron-based SAXS instrument where they could yield even higher performance enhancements with the incident beam intensity. (Li *et al.*, 2008). Extendable vacuum pipes sealed with Kapton windows are attached to the beamline to minimize the air gap around the sample position to a few centimeters and to keep the background scattering from air to a minimum, aided by motorized (Tx, Tz) sample stages with 1 micron resolution over a 100 mm range of motion. As radiation damage to samples, and even more especially for solution, may result in the formation of aggregates can cause significant problems at high-brilliance synchrotron source, the MARS beamline is equipped with a beam attenuator composed of 8 pneumatic holders for aluminum foils of 0.05 mm to 8.0 mm thicknesses allowing a fine tune of the beam attenuation to achieve the optimal balance between lowering useful signal and reducing the effects of radiation damage.

Finally, a crucial step in SAXS data processing is the subtraction of the sample environment scattering from that of the sample, and these two independent patterns must be appropriately normalized to consider possible variation in the beam flux and differences in transmission. This operation can be conveniently accomplished by using an active beamstop. A miniature 3 mm x 2 mm active beamstop using a pin diode has been developed internally at SOLEIL. The beamstop has been shaped by additive manufacturing by tungsten laser powder bed fusion that made us possible to produce this complex functional component in a resource-efficient and economical manner. The beamstop is installed into the He-flushed flight tube ended by a 345 mm-diameter Kapton window at the SAXS detector. The flight tube is positioned into the beam by motorized (Tx, Tz) stages. The “integration” detector is a MAR-Research system with a sensitive phosphor imaging surface diameter of 345 mm. (**Figure 2**)

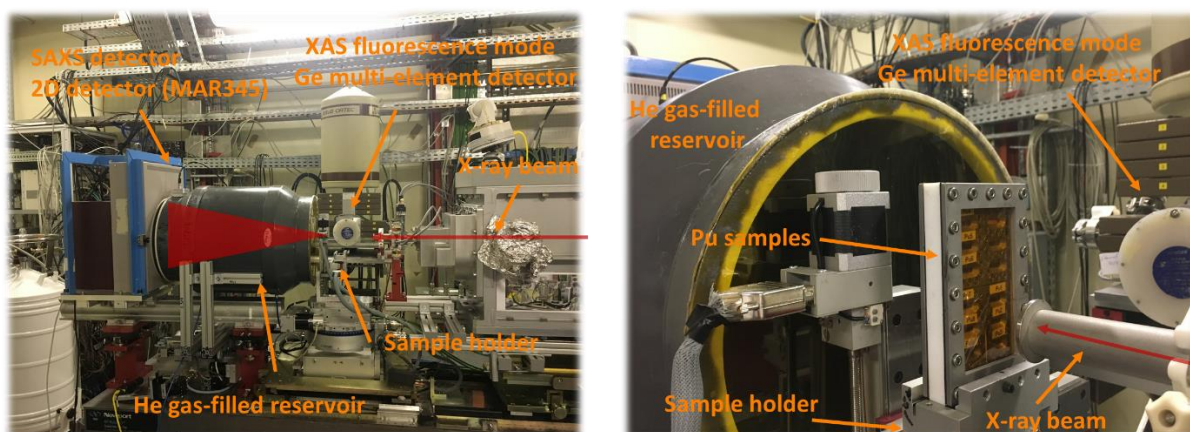


Figure 2 : MARS Beamline CX3 end-station configuration to perform combined SAXS-XAS analyses.

Combined Small Angle X-ray Scattering (SAXS) and X-ray Absorption Spectroscopy (XAS) analyses were performed with the storage ring operating in top-up mode at an electron current of 500 mA, 2.5 GeV. Beam energy calibration was performed at the Yttrium K-edge corresponding to 17.038 keV. The focused beam size on sample was $300\ \mu\text{m} \times 400\ \mu\text{m}$ (**Figure 2**). A specific cell was used for radioactive samples and was composed of Teflon sample holders containing three slots of $250\ \mu\text{L}$ closed by two layers of Kapton® films (polyimide) on each side. Reproduced from (Micheau *et al.*, 2020) with permission from the Royal Society of Chemistry.

Small Angle X-ray Scattering (SAXS).

SAXS experiments were carried out using the 2D image plate detector (MAR345, marXperts GmbH, Germany), with an X-ray energy of 17 keV corresponding to an average wavelength of $0.7294\ \text{\AA}^{-1}$, and a sample to detector distance of 785.70 mm. The calibration of the angular axis was made by the powder diffraction pattern of silver behenate. This configuration allows covering a Q-range between about $0.1\ \text{nm}^{-1}$ and $18.8\ \text{nm}^{-1}$. Sample transmissions were recorded during 10 s using photodiodes and scattering diagrams were recorded during 5 s per sample. Isotropic 2D scattering data were azimuthally averaged to obtain the scattering intensity $I(Q)$ using Fit2D software. (Hammersley *et al.*, 1996) Sample scattering intensity was then normalized by the acquisition time, transmission and thickness, and multiplied by a normalization constant determined with the help of the scattering intensity of polyethylene (PE) at $Q = 0.36\ \text{nm}^{-1}$ that corresponds to $4.9\ \text{cm}^{-1}$. The absolute intensity scattered by the cluster was finally obtained by subtracting the empty cell, solvent and background contributions. Data were simulated using the SasView 4.2.0 software (<http://www.sasview.org>) especially for core-shell, lamella and disk form factors.

Pu L_3 -edge X-ray Absorption Spectroscopy (XAS)

Experimental spectra were recorded in fluorescence mode using a Ge multi-element detector (ORTEC, Oak Ridge, Tennessee, USA) at the Pu L₃-edge. The samples were oriented at 45° with respect to the incident beam. The incident energy was calibrated using a metallic Zr foil (K-edge defined at 17.988 keV). Pu ionization energy was defined at the maximum of the white line and corresponds to 18.068 keV. The spectrum corresponds to the average of 6 pre-processing scans obtained after 60 min of analysis each. EXAFS data were analyzed with Athena and Artemis software from the IFEFFIT package. (Ravel & Newville, 2005) Data fitting was performed using a Keiser-Bessel window with a cluster size of 1-5 Å for the Fourier Transform (FT) in the 2 Å < k < 14 Å range (Feff version 8.4). Two parameters were fitted: atomic distances (R), and Debye-Waller factor (DWF). Coordination numbers are fixed to the crystal structure value.

Results

The SAXS data processing operations performed on the signal acquired on the plutonium cluster are summarised in the **Figure 3**. The raw data curves gathered in Figure 3.a. correspond to the signal obtained on the sample and an empty cell as a reference. Both diagrams exhibit a well defined peak at 4 nm⁻¹ which is attributed to the scattering of the 4 Kapton® layers on the sample cell. This peak is still visible after the empty cell subtraction, as can be seen in the **Figure 3.b** where the pure solvent and the sample are compared after normalization of the data according to the sample thickness, transmission, acquisition time and scattering intensity of polyethylene (PE) used as a reference. The residual presence of the Kapton® peak can be attributed to the non-reproducible handmade cell and to the impossibility of measuring the exact empty cell used for the radioactive sample. Nevertheless, the observation of both diagrams demonstrate a significant scattering difference when comparing the hexanuclear cluster and the solvent, particularly around 10⁰ nm⁻¹. The absolute intensity scattered by the cluster is shown on **Figure 3.c**. after subtracting the solvent contribution while considering the total conversion of Pu(IV) into DOTA polyamino carboxylate PuO₂ clusters (corresponding to a volume fraction of 0.018). Note that a subtraction artifact related to the Kapton® is still visible at 4 nm⁻¹. Small intensity variation are also observed at low Q vector. This can be attributed to a subtraction artifact due to the low scattering intensity of such dilute samples, or to a structure factor linked to cluster interaction or aggregation. Further investigation at higher concentration are planned in order to investigate this diagram region. Nevertheless, the normalised SAXS diagram of the plutonium clusters (**Figure 2.c**) in absolute unit can be fitted using simple fitting models. This diagram displays a Q⁰ slope at low wave vector and tends to a Q⁻⁴ slope at higher wave vectors which behaviour is a typical signature of three dimensional and compact objects with a sharp interface.

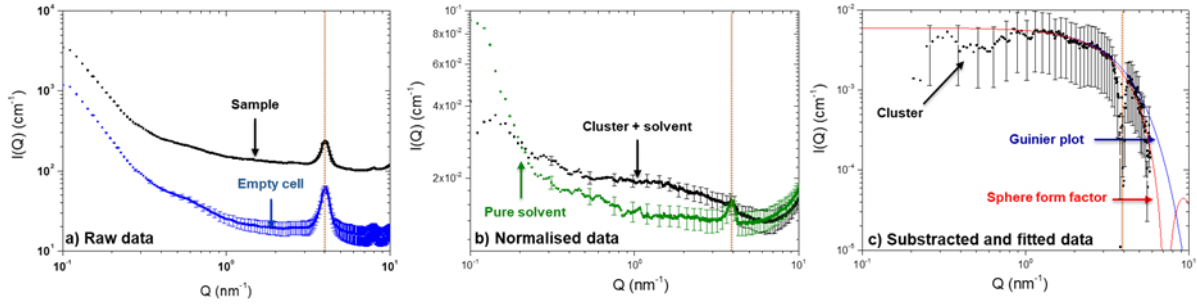


Figure 3. SAXS data of the plutonium clusters solution at different processing steps: a) raw data of the sample (black) and empty cell (light blue) in arbitrary unit (a.u.); b) Normalized data in absolute unit after empty cell subtraction for the cluster sample (black) and the pure solvent (green); and c) cluster signal (black) after solvent contribution subtraction and fit models: Sphere form factor (red line) and Guinier plot (dark blue line). The vertical dot line in each graph corresponds to the expected position of the Kapton® scattering peak.

The scattering intensity is generally described as the product between an initial intensity I_0 (when Q tends to 0), a form factor $P(Q)$ relative to the shape of the solute, and a structure factor $S(Q)$ related to the interaction between solutes. (O. Glatter and O. Kratky, Small angle x-ray scattering, Academic Press, London, New York, 1982) At the first approximation, and considering a very dilute solution, $S(Q)$ is considered equal to 1. Two approaches were employed in the $1 - 6 \text{ nm}^{-1}$ Q range to determine the size of the plutonium clusters: (i) Guinier analysis, and (ii) a monodisperse sphere form factor fitting (Fig. 2c). In these two models, the initial intensity I_0 is defined as follows (Eq. (1)).

$$I_0 = \varphi_c V_c \Delta\rho^2 \quad (\text{Eq. 1})$$

with φ_c , the volume fraction of the clusters, V_c , the volume of one cluster and $\Delta\rho^2$, the scattering length density contrast with the solvent. **Table 1** summarizes the scattering length density ρ_c and the contrast $\Delta\rho^2$ used for the calculations.

Table 1: X-ray scattering length density (ρ_c) and electron contrast ($\Delta\rho^2$) used for SAXS diagram simulation calculations. Values for plutonium cluster takes into account both organic volume of the DOTA polyamino carboxylate ligands and the $[\text{Pu}_6(\text{OH})_4\text{O}_4]^{12+}$ core.

	$\rho_c (10^{10} \text{ cm}^{-2})$	$\Delta\rho^2 (10^{20} \text{ cm}^{-4})$
Pu cluster	13.5	Pu cluster/H ₂ O 16.6
H ₂ O	9.43	

The Guinier analysis gives a first estimation of the cluster radius of gyration R_g . A radius of gyration of ca. 0.48 nm is found. Considering spherical and filled entities, the radius of the cluster can be deduced

with the following equation (Eq. (2)) where R is the radius of the sphere. This leads to a sphere radius of 0.62 nm (*cf.* 1.22 nm diameter).

$$R_g = R\sqrt{(3/5)} \quad (\text{Eq. 2})$$

The best fits obtained with the monodisperse sphere form factor model is consistent with a sphere radius R of about 0.62 nm which is in full agreement with the results obtained with the Guinier analysis. The fitting parameters are summarised in **Table 2**.

Table 2: Simulated results of SAXS diagrams obtained with SasView software: I_0 is the intensity for $Q \rightarrow 0$, R_g the gyration radius, and R the radius of the sphere.

Sample information		Model		
Name	I_0 (cm ⁻¹)	R_g (nm)	R (nm)	Sphere R (nm)
Pu cluster	0.006±0.003	0.48±0.05	0.62±0.05	0.62±0.06

Finally, both models conclude in the description of the cluster as quite spherical particles measuring 1.2 nm in diameter in nitric solution. The size probed with SAXS approach using a monodisperse sphere form factor may be compared to the one expected from the crystallographic data of the plutonium hexanuclear clusters (Tamain *et al.*, 2016). The $[\text{Pu}_6(\text{OH})_4\text{O}_4(\text{H}_2\text{O})_8(\text{HDO})_4]$ complex is made of a $[\text{Pu}_6(\text{OH})_4\text{O}_4]^{12+}$ core decorated with four DOTA polyamino carboxylate ligands which forms an oblate spheroid with a 0.45 nm radius in the axial direction and 0.8 nm radius in the equatorial direction (**Figure 4**). Indeed the value obtained using a sphere form factor of 0.62 is intermediate between the two values and appears to be a good geometrical approximation. A more accurate approximation of the overall cluster shape in solution would involve more sophisticated geometry and electron contrast models. However, in this experiment, the experimental SAXS signal does not allow such a precise description. With a better normalization that suffer less from the sample holder scattering signal, this limit may be overcome with an optimized set-up in future works.

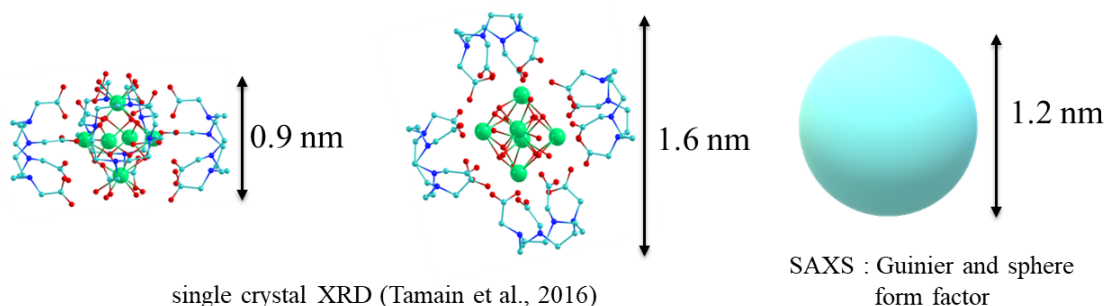


Figure 4 : Comparison of the SAXS Guinier and sphere form factor models to the $[\text{Pu}_6(\text{OH})_4\text{O}_4(\text{H}_2\text{O})_8(\text{HDO}^-\text{TA})_4]$ complex structure from single crystal XRD (Tamain *et al.*, 2016). The complex structure, in the solid state, shows the anisotropic DOTA complexation on the octahedral $[\text{Pu}_6(\text{OH})_4\text{O}_4]^{12+}$ core which results in an oblate spheroid.

Previous X-ray absorption spectroscopy measurements carried on the plutonium solution demonstrated the existence of the plutonium cluster as a soluble species. The clusters are made of six plutonium centers that form an octahedron, which are connected by oxo and hydroxo bonds alternating on each faces of the octahedron and carboxylate functions that bonds along the octahedron edges. The k^3 weighted EXAFS oscillations and its corresponding Fourier Transform (FT) acquired from this experiment are presented in the **Figure 4**. The overall shape of the FT is consistent with previous measurements made on similar samples. Low frequency contributions at $k < 7 \text{ \AA}^{-1}$ correspond to the plutonium-oxygen coordination sphere ($1 \text{ \AA} < R+\phi < 2 \text{ \AA}$ in the FT). High frequency oscillations at $k > 7 \text{ \AA}^{-1}$ are dominated by a heavy backscatterer which evidences a plutonium polynuclear species. An intermediate contribution observed between $R+\phi = 2.2$ and 3.2 \AA in the FT originates from carboxylate carbon atoms.

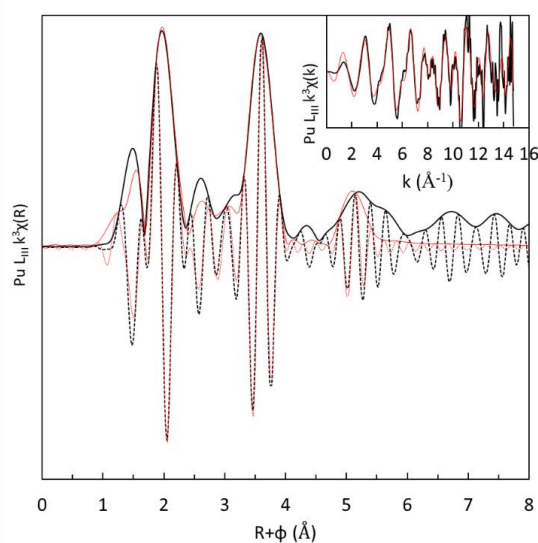


Figure 4. Fourier Transform of the k^3 weighted EXAFS spectra (black lines) and best fit results (red lines) of the plutonium solutions prepared by dissolution of Pu(IV) hexanuclear cluster crystals. k^3 weighted EXAFS oscillations and fits are presented in the insert and the imaginary part of the Fourier Transform are the black and red dashed lines.

The best fit spectra (red lines on **Figure 4 and Table 3**) were obtained using the crystal structure already published, (Tamain *et al.*, 2016) and are in excellent agreement with the experimental data. In the fit

procedure, distances, Debye-Waller Factors (DWF), the amplitude reduction factor (S_0^2) and the energy shift (E^0) were refined while the coordination numbers were fixed according to the crystal structure. In agreement with the latter, the first actinide coordination shell is well reproduced by two distinct Pu-O subshell. The first one corresponds to two capping $\mu_3\text{-O}^{2-}$ oxygens at a distance of 2.18 Å (± 0.01 Å). The second Pu-O subshell at 2.40 Å contains the other six Pu-O distances ($\mu_3\text{-OH}^-$, water molecules and O from carboxylate functions). As this sub-shell contains different type of bonds and distances, the Debye Waller Factor (DWF) is large (0.008 Å²) in comparison to the short oxygen shell (0.004 Å²). Considering the hexanuclear cluster geometry, the Pu-Pu signal splits into two shells. The edge sharing shell consist in four Pu-Pu scattering path with a 3.77 Å bond length. A longer bond corresponds to the opposite Pu atoms in the octahedron at 5.31 Å. Overall, all parameters are fully consistent with previous reports on this type of hexanuclear complexes and agrees well with the crystallographic structure.

Table 3: EXAFS refined metrical parameters obtained for the best fit of the soluble Pu-DOTA hexanuclear clusters.

$E_0 = -0.9(20)$ eV $S_0^2 = 0.75(15)$	An- $\mu_3\text{O}^{2-}$	An-($\mu_3\text{OH}^-$, O _c , H ₂ O)	An-C	An-An1	An-An2
CN*	2*	6*	2*	4*	1*
σ^2 (Å ²)	0.004(2)	0.008(2)	0.003(4)	0.006(2)	0.003(3)
R (Å)	2.18(2)	2.40(2)	3.35(3)	3.77(2)	5.3(3)
R_{XRD} (Å)	2.20	2.36	3.34	3.76	5.31

Errors in brackets only reflect the mathematical uncertainty provided by the proposed model.

* : fixed values

Conclusion

The characterization of the Pu(IV) hexanuclear cluster using synchrotron SAXS coupled with EXAFS undertakes an analytical challenge to describe actinide coordination mode and structure in dilute solutions. These species are of great interest for obvious environmental reasons and require a thorough characterization and speciation. Spectroscopic techniques as well as crystallographic characterization initially paved the way in this sense. In this experiment, we extend our knowledge on these compounds by combining synchrotron X-ray scattering and absorption techniques. The synthesis of the hexanuclear cluster was controlled by UV-visible-NIR spectroscopy and the EXAFS analyses were fully consistent with previous results. The SAXS identify 1.2 nm diameter spherical particles in good agreement agreeing with the shape of the $[\text{Pu}_6(\text{OH})_4\text{O}_4(\text{H}_2\text{O})_8(\text{HDOTA})_4]$ complex described previously by single crystal XRD.

The instrumental setup description fulfils the expectations of users for measuring highly radioactive samples in environmental dilute conditions even for weakly scattering clusters. Nevertheless, the instrument is being further developed. Thus, the MARS beamline is equipped with a Pilatus 3 2M (Dectris, Switzerland) hybrid photon-counting pixel detector having practically no detector readout noise, a high dynamic range and a short readout time. It is mounted on a new (Tx, Ts, Rx) motorized support to form camera lengths anywhere from 0.35 m to 3 m in 0.25m steps. On the SAXS camera nosecone, a second detector affording partial 2-dimensionnal access to Wide Angle X-ray Scattering (WAXS) information will be operated to complement full 2D SAXS in the appropriate configuration. With careful beamline set up, these detectors allow overlap of the reduced 1D SAXS and WAXS data over the full camera length capability of the beamline. Thus, any reasonable size sample environment can be accommodated whilst minimizing air gaps and attendant background scatter. To capitalize on the energy tunability of the beamline, anomalous SAXS might be exploited to probe changes of the scattering properties of selected atoms to gain information on the distribution of the resonant atoms within the sample.

Acknowledgements

We gratefully acknowledge Hervé Hermange for his fruitful assistance in the mechanical design and integration of the active beamstop and fitting of the SAXS setup on the CX3 end-station of the MARS beamline. This work was supported by the CEA through the chemistry research program (RCHIM) from the cross-cutting basic research program (RTA).

References

- Altmaier, M., Gaona, X. & Fanghanel, T. (2013). *Chem Rev* **113**, 901-943.
- Bechade, J. L., Menut, D., Doriot, S., Schlutig, S. & Sitaud, B. (2013). *J Nucl Mater* **437**, 365-372.
- Bechade, J. L., Menut, D., Lescoat, M. L., Sitaud, B., Schlutig, S., Solari, P. L., Llorens, I., Hermange, H., de Carlan, Y., Ribis, J. & Tualbi, L. (2012). *J Nucl Mater* **428**, 183-191.
- Bengio, D., Dumas, T., Arpigny, S., Husar, R., Mendes, E., Solari, P. L., Schlegel, M. L., Schlegel, D., Pellet-Rostaing, S. & Moisy, P. (2020). *Chem-Eur J* **26**, 14385-14396.
- Dalodiere, E., Virost, M., Morosini, V., Chave, T., Dumas, T., Hennig, C., Wiss, T., Blanco, O. D., Shuh, D. K., Tylliszczak, T., Venault, L., Moisy, P. & Nikitenko, S. I. (2017). *Sci Rep-Uk* **7**.
- Dembowski, M., Colla, C. A., Yu, P., Qiu, J., Szymanowski, J. E. S., Casey, W. H. & Burns, P. C. (2017). *Inorg Chem* **56**, 9602-9608.
- Dumas, T., Guigue, M., Moisy, P., Colina-Ruiz, R., de Leon, J. M., Matara-Aho, M., Solari, P. L., Monfort, M., Moulin, C., Beccia, M. R. & Den Auwer, C. (2018). *Chemistryselect* **3**, 2021-2024.
- Falaise, C., Neal, H. A. & Nyman, M. (2017). *Inorg Chem* **56**, 6591-6598.
- Falaise, C. & Nyman, M. (2016). *Chem-Eur J* **22**, 14678-14687.
- Geckeis, H., Lutzenkirchen, J., Polly, R., Rabung, T. & Schmidt, M. (2013). *Chem Rev* **113**, 1016-1062.
- Gerber, E., Romanchuk, A. Y., Pidchenko, I., Amidani, L., Rossberg, A., Hennig, C., Vaughan, G. B. M., Trigub, A., Egorova, T., Bauters, S., Plakhova, T., Hunault, M. O. J. Y., Weiss, S., Butorin, S. M., Scheinost, A. C., Kalmykov, S. N. & Kvashnina, K. O. (2020). *Nanoscale* **12**, 18039-18048.
- Hammersley, A. P., Svensson, S. O., Hanfland, M., Fitch, A. N. & Hausermann, D. (1996). *High Pressure Res* **14**, 235-248.

- Hennig, C., Takao, S., Takao, K., Weiss, S., Kraus, W., Emmerling, F. & Scheinost, A. C. (2012). *Dalton T* **41**, 12818-12823.
- Hennig, C., Weiss, S., Kraus, W., Kretzschmar, J. & Scheinost, A. C. (2017). *Inorg Chem* **56**, 2473-2480.
- Kersting, A. B., Efurud, D. W., Finnegan, D. L., Rokop, D. J., Smith, D. K. & Thompson, J. L. (1999). *Nature* **397**, 56-59.
- Knope, K. E. & Soderholm, L. (2013). *Inorg Chem* **52**, 6770-6772.
- Knope, K. E., Wilson, R. E., Vasiliu, M., Dixon, D. A. & Soderholm, L. (2011). *Inorg Chem* **50**, 9696-9704.
- Li, Y. L., Beck, R., Huang, T., Choi, M. C. & Divinagracia, M. (2008). *J Appl Crystallogr* **41**, 1134-1139.
- Llorens, I., Solari, P. L., Sitaud, B., Bes, R., Cammelli, S., Hermange, H., Othmane, G., Safi, S., Moisy, P., Wahu, S., Bresson, C., Schlegel, M. L., Menut, D., Bechade, J. L., Martin, P., Hazemann, J. L., Proux, O. & Den Auwer, C. (2014). *Radiochim Acta* **102**, 957-972.
- Marsac, R., Banik, N. L., Marquardt, C. M. & Kratz, J. V. (2014). *Geochim Cosmochim Acta* **131**, 290-300.
- Martin, N. P., Volkringer, C., Henry, N., Trivelli, X., Stoclet, G., Ikeda-Ohno, A. & Loiseau, T. (2018). *Chem Sci* **9**, 5021-5032.
- Menut, D., Bechade, J. L., Cammelli, S., Schlutig, S., Sitaud, B. & Solari, P. L. (2015). *J Mater Res* **30**, 1392-1402.
- Micheau, C., Virot, M., Dourdain, S., Dumas, T., Menut, D., Solari, P. L., Venault, L., Diat, O., Moisy, P. & Nikitenko, S. I. (2020). *Environ Sci-Nano* **7**, 2252-2266.
- Neck, V., Altmaier, M., Seibert, A., Yun, J. I., Marquardt, C. M. & Fanghanel, T. (2007). *Radiochim Acta* **95**, 193-207.
- Ravel, B. & Newville, M. (2005). *J Synchrotron Radiat* **12**, 537-541.
- Sitaud, B., Solari, P. L., Schlutig, S., Llorens, I. & Hermange, H. (2012). *J Nucl Mater* **425**, 238-243.
- Takao, K., Takao, S., Scheinost, A. C., Bernhard, G. & Hennig, C. (2012). *Inorg Chem* **51**, 1336-1344.
- Tamain, C., Dumas, T., Guillaumont, D., Hennig, C. & Guilbaud, P. (2016). *Eur J Inorg Chem* 3536-3540.
- Tamain, C., Dumas, T., Hennig, C. & Guilbaud, P. (2017). *Chem-Eur J* **23**, 6864-6875.
- Walther, C., Cho, H. R., Marquardt, C. M., Neck, V., Seibert, A., Yun, J. I. & Fanghanel, T. (2007). *Radiochim Acta* **95**, 7-16.
- Walther, C. & Denecke, M. A. (2013). *Chem Rev* **113**, 995-1015.
- Zhang, J. Q., Tian, Q., Li, Q. T., Henderson, M. J., Tuo, X. G., Yan, M. H. & Almsy, L. (2019). *J Mol Liq* **296**.